PAPER

Check for updates

Controlled synthesis of metal–insulator–metal nanoparticles for enhanced Raman spectroscopy

Junhu Zhou, [ID] [a] Xin Qi [ID] *[b] and John X. J. Zhang*[a]

Surface-enhanced Raman spectroscopy (SERS) is a powerful spectroscopic technique offering non-destructive and ultra-sensitive molecular characterization. Reliable SERS signals are typically generated using patterned metal surfaces or metal nanoparticles, primarily composed of gold (Au) and silver (Ag). However, the extreme spatial confinement required to form these hotspots (less than 5 nm) necessitates a complex fabrication process. Here, we present a novel approach, termed metal–insulator–metal (MIM) nanoparticle-enhanced Raman spectroscopy, which achieves robust Raman signal amplification through nanoparticles comprising a gold core, an ultrathin silica insulating layer, and surface gold satellites. The ultrathin silica layer prevents aggregation, enabling the formation of active SERS regions both between gold nanoparticles and on the outer surface. This configuration provides high-quality SERS spectra for liquid samples without requiring patterned substrates or stringent nanoparticle manipulation. The optimal MIM structure is determined by Finite Element Analysis (FEA) with a 120 nm gold core, a 3 nm silica layer, and a 13 nm surface gold nanoparticle. The detection limit of ciprofloxacin using the MIM nanoprobe is 1 pg mL^{-1}. By incorporating theory-guided structure-controlled synthesis, our method significantly enhances the versatility and accessibility of SERS, paving the way for transformative applications in materials science, life sciences, and environmental monitoring.

Introduction

The detection of organic molecules is essential in various fields, including medical diagnostics,[1] environmental monitoring,[2] food safety,[3] and chemical analysis.[4] Sensitive and accurate molecular detection plays a crucial role in identifying trace amounts of target analytes, enabling early disease diagnosis, contamination assessment, and biochemical research. Various detection techniques have been developed to achieve high sensitivity and specificity, such as fluorescence-based assays, mass spectrometry, and electrochemical sensors.[5–7] However, these methods often require complex sample preparation or expensive instrumentation, or suffer from limited molecular specificity.

Raman spectroscopy, a vibrational spectroscopy technique, is widely used to analyze the molecular composition and structure.[8] It works by shining a laser onto a sample and measuring the scattered light that undergoes an energy shift due to interactions with molecular vibrations. However, conventional Raman spectroscopy suffers from inherently weak signal intensity due to the extremely low probability of Raman scattering.[9] To overcome this limitation, surface-enhanced Raman spectroscopy (SERS) has been developed, which leverages the plasmonic effect of metallic nanostructures to amplify Raman signals by several orders of magnitude.[9,10] Plasmonic metal nanoparticles, such as gold and silver, exhibit a unique localized surface plasmon resonance (LSPR) caused by the collective oscillation of free electrons on their surfaces when excited by incident light at specific wavelengths, and this resonance generates an enhanced local electric field, which significantly boosts Raman signal intensity.[11] Studies have shown that extremely narrow gaps (<5 nm) between metallic nanostructures, known as "hot-spots", can dramatically enhance Raman signals by several orders of magnitude.[12]

Despite its high sensitivity, SERS-based sensing still faces challenges in achieving reliable quantitative analysis, particularly for detecting target analytes at ultralow concentrations. A major limitation arises from the stochastic nature of SERS signals, which results from the spatial non-uniformity of hotspot distributions and the dynamic adsorption of molecules onto the sensing surface.[13,14] These fluctuations result in variations in the measured Raman intensity, thereby reducing the accuracy and reproducibility of quantitative SERS detection. While functionalization strategies can immobilize target molecules near hotspots, they cannot fully eliminate signal variability caused by molecular orientation and positional uncertainty.[15,16] Therefore, it is critical to design hotspot patterns with uniform density and maximized intensity. Traditional approaches for hotspot optimization fall into two

aThayer School of Engineering, Dartmouth College, Hanover, NH 03755, USA.
E-mail: John.Zhang@Dartmouth.edu
bDepartment of Chemistry, Dartmouth College, Hanover, NH 03755, USA.
E-mail: Xin.Qi@dartmouth.edu

major categories: nanoparticle-based and substrate-based configurations. Nanoparticle-based sensors leverage closely packed nanostructures such as colloidal nanoparticle clusters,[17] DNA-origami-assembled dimers,[18,19] and core–shell nanoparticle architectures.[20] However, the controlled synthesis of nanomaterials with desired hotspot locations and electric field distribution remains challenging, leading to signal inconsistency. On the other hand, substrate-based SERS sensors, which utilize uniform nanopatterned surfaces fabricated *via* techniques such as photolithography and deposition, offer improved signal uniformity but suffer from issues such as the coffee-ring effect, where nonuniform analyte distribution reduces measurement accuracy.[21,22] The success and limitations of these approaches suggest that the development of a SERS sensor with reduced signal variation and improved quantification reliability remains a critical research goal.

Recent advancements have addressed some of these challenges. Highly homogeneous nanoparticles with controlled sizes and geometries have been synthesized, enhancing reproducibility in SERS measurements.[23] Additionally, digital SERS protocols employing single-molecule counting have improved signal reproducibility by converting analog signals into digital counts, thereby reducing variability.[17] In this work, we combine simulation, theory, and experiment to address these challenges, particularly in designing and synthesizing SERS nanosensors with optimized hotspots. We first used finite element analysis (FEA) simulations to design a metal–insulator–metal (MIM) nanoparticle-based plasmonic nanosensor with optimized enhancement structures. We then employed colloidal theory to develop a controlled synthesis and self-assembly strategy for fabricating MIM nanoparticles with desired sizes, shell thickness, and final MIM assembly structures. Unlike traditional SERS probes that rely on nanoparticle clustering for hotspot formation, our rational design approach allows each individual MIM nanoparticle to function as an independent SERS sensor, offering enhanced reproducibility and reliability. Our MIM molecular sensor demonstrated superior detection sensitivity, achieving a detection limit as low as 1 pg mL^{-1} for ciprofloxacin, a widely used antibiotic, through a digital counting calibration approach. This work represents the first realization of a MIM-based SERS probe that operates independently without requiring nanoparticle aggregation, marking a significant advancement in quantitative SERS sensing. The proposed MIM nanoparticle sensor offers a robust, reproducible, and highly sensitive molecular detection platform, with broad potential applications in liquid-phase chemical analysis, biomedical diagnostics, and environmental monitoring.

Materials and methods

Materials

Chloroauric acid (HAuCl$_4$·xH$_2$O, 99.995%), trisodium citrate dihydrate (99%), sodium borohydride (NaBH$_4$, 98%), potassium carbonate (K$_2$CO$_3$, 99%), sodium hydroxide (NaOH, 97%),

hydroxylamine hydrochloride (NH$_2$OH·HCl, 99%), (3-aminopropyl)triethoxysilane (APTES, 98%), (3-aminopropyl)trimethoxysilane (APTMS, 97%), sodium silicate solution (10.6% Na$_2$O, 26.5% SiO$_2$), hydrochloric acid (37%), and 4-nitrothiophenol (4-NTP, 80%) were purchased from Sigma Aldrich. All the materials were used without additional purification. Deionized (DI) water with a resistivity of 18.3 MΩ cm was used in the experiments.

COMSOL Multiphysics® simulations

The 3D geometry of the MIM nanoparticle is shown in Fig. S1A, where the outer cubic box represents a perfectly matched layer (PML) used to truncate the computational domain and eliminate artificial reflections. The incident plane-polarized electromagnetic wave enters from one port and exits through the opposite face of the simulation domain (Fig. S1B). The meshing scheme was set to physics-controlled (fine setting) to ensure computational accuracy (Fig. S1C), while Fig. S1D illustrates the detailed meshing of the MIM nanoparticle. The final mesh consisted of 329 125 domain elements, 42 820 boundary elements, and 5393 edge elements. A parametric sweep was conducted for incident light wavelengths ranging from 450 nm to 900 nm in increments of 10 nm.

MIM nanoparticle synthesis

Synthesis of gold nanoparticles (AuNPs). Exterior AuNPs (~13 nm in diameter) were synthesized using the Turkevich method by rapidly injecting 5 mL of sodium citrate solution (38.8 mM) into 50 mL of boiling chloroauric acid solution (1 mM) under vigorous stirring at 1150 rpm.[24,25] The solution was boiled for 30 min and then allowed to cool to room temperature.

Core AuNPs (~60 nm in diameter) were synthesized by injecting 0.65 mL of sodium citrate solution (10 mg mL^{-1}) into 100 mL of boiling chloroauric acid solution (0.1 mg mL^{-1}) under vigorous stirring at 1150 rpm. The solution was boiled for 30 min before cooling to room temperature.

Larger core AuNPs (~90 nm and ~120 nm in diameter) were synthesized using a seed-mediated growth method.[26] Au seeds of ~40 nm were first synthesized by rapidly injecting 1 mL of sodium citrate solution (10 mg mL^{-1}) into 100 mL of boiling chloroauric acid solution (0.1 mg mL^{-1}) under vigorous stirring at 1150 rpm. The solution was boiled for 30 min and then cooled to room temperature. To grow larger particles, 4 mL of the 40 nm Au seed solution was added to 53 mL of DI water, followed by the addition of 0.9 mL of sodium citrate solution (10 mg mL^{-1}). The reaction was continued by adding either 0.9 mL (for ~120 nm AuNPs) or 0.36 mL (for ~90 nm AuNPs) of chloroauric acid solution (0.1 mg mL^{-1}) under stirring for 10 min. Finally, 1.4 mL of hydroxylamine hydrochloride solution (10 mM) was added dropwise under vigorous stirring at 1150 rpm.

Ultrathin silica coating. Silica coating was applied using a two-step process adapted from previous research, involving surface activation with silane agents (APTES or APTMS), fol-

lowed by silica deposition using sodium silicate in aqueous solution.[26,27] For surface activation, 15 mL of core AuNP solution was diluted to 30 mL, and 0.5 mL of the silane agent was added under vigorous stirring for at least 20 min. Specifically, APTES (0.5 mM) was used for 120 nm and 90 nm AuNPs, while APTMS (1 mM) was used for 60 nm AuNPs. Silica deposition was performed by adding sodium silicate solution (diluted to 0.54% (wt/wt) with DI water and adjusted to pH ~10) in the following volumes: 2.8 mL for 120 nm AuNPs, 2.2 mL for 90 nm AuNPs, and 1.6 mL for 60 nm AuNPs. The mixture was then placed in a 90 °C water bath under stirring for 40 min. After the reaction, the solution was centrifuged at 2000g for 10 min and washed twice with DI water.

Silica surface functionalization with APTES. To ensure a positively charged surface, the silica-coated AuNPs were functionalized with APTES. A stock solution of APTES (12 mM) was prepared in an $EtOH : H_2O$ (3 : 1, v/v) mixture. One milliliter of silica-coated AuNP solution was added to 12 mL of APTES stock solution and incubated in a 95 °C water bath under vigorous stirring for 1 hour. After cooling to room temperature, the solution was centrifuged at 2000g for 10 min and washed twice with DI water.

Assembly of MIM nanoparticles. Immediately after APTES grafting, the silica-coated AuNPs were mixed with exterior AuNPs (~13 nm) at a volume ratio of 10 : 1 under gentle stirring at 200 rpm at room temperature for at least 2 hours to facilitate self-assembly. The assembled MIM nanoparticles were collected by centrifugation at 1200g for 10 min and washed twice with DI water.

Assembly of MIM nanoparticles with $NaBH_4$-stabilized AuNPs. A second $NaBH_4$-stabilized assembly approach, adapted from previous work, was employed.[28,29] To initiate the reaction, 0.5 mL of APTES-treated silica-coated AuNP solution was added to 10 mL of chloroauric acid solution (10 mM), and the pH was adjusted to ~7 using 0.1 M NaOH. The mixture was then heated in a 75 °C water bath under stirring for 10 min and subsequently cooled to room temperature. Following this step, 100 mL of K_2CO_3 solution (280 µg mL^{-1}) and 50 mL of chloroauric acid (1 mM) were sequentially added under stirring. To complete the nanoparticle formation, 5 mL of freshly prepared ice-cold $NaBH_4$ solution (10 mM) was rapidly injected under vigorous stirring. The solution was stirred for 10 min and left to stand for 2 hours. Finally, the MIM nanoparticles were collected by centrifugation at 1200g for 10 min and washed twice with DI water.

Material characterization

Scanning electron microscopy (SEM) was performed using an FEI Helios 5CX dual-beam scanning electron microscope operating at 20 kV and 21 pA. Transmission electron microscopy (TEM) and energy-dispersive X-ray spectroscopy (EDS) were carried out on a Thermo Scientific Talos F200i S/TEM at an accelerating voltage of 200 kV. Optical absorbance spectra were measured using a Tecan Spark 10M multimode plate reader. Raman spectra were recorded with a HORIBA LabRAM AFM-Raman spectrometer.

SERS measurements

SERS measurements were conducted in a liquid-phase system. 10 µL of ciprofloxacin solution was mixed with 100 µL of MIM nanoparticle solution, followed by 1 min of sonication to ensure uniform dispersion. A 10 µL portion of the resulting mixture was then deposited onto a clean glass coverslip, and a second coverslip was placed on top to create a thin liquid layer. This configuration was carefully positioned under the Raman spectrometer's objective lens, with the focal plane precisely adjusted to the center of the liquid layer for optimal signal acquisition. SERS spectra were collected in a point-by-point mapping mode using a 633 nm laser (Melles Griot 05-LPL-915-070, W_{max} = 40 mW, 10% intensity) as the excitation source, with a grating parameter of 300 grooves per mm. The acquisition time was set to 500 ms per point. A 50× lens (NA = 0.75) was used to collect the signals. The diameter of the focused spot was approximately 1 µm $\left(\frac{1.22 \times 0.633}{0.75} \right)$.

Results and discussion

In this work, we designed and synthesized a new MIM nanoparticle configuration for SERS applications to address the limitations of conventional plasmonic sensors. While previous research has achieved significant advancements in synthesizing homogeneous nanoparticles with controlled sizes and geometries, as well as improving signal reproducibility through digital SERS protocols for liquid samples, challenges remain in achieving consistent and reproducible hotspot formation without relying on nanoparticle aggregation. Our MIM structure addresses these challenges by employing a rationally designed plasmonic enhancement mechanism on the exterior gold nanoparticle (AuNP) surfaces, enabling each nanoparticle to function as an independent SERS sensor. To investigate the plasmonic enhancement characteristics of the MIM configuration, we performed finite element analysis (FEA) simulations using COMSOL Multiphysics® to compute the local electric field distribution. Rather than directly simulating the Raman signal at the molecular level, we analyzed the electric field intensity, given that the SERS enhancement factor (EF) is approximately proportional to the fourth power of the local electric field enhancement:[11]

$$EF = \frac{|E_{loc}(\omega_0)|^2 |E_{loc}(\omega_R)|^2}{|E_0(\omega_0)|^2 |E_0(\omega_R)|^2} \approx \left| \frac{E_{loc}(\omega_R)}{E_0(\omega_0)} \right|^4 \quad (1)$$

where ω_0 and ω_R represent the incident and Raman-scattered frequencies, respectively, and E_{loc} and E_0 are the local and incident electric fields. Since the SERS enhancement is fundamentally linked to the local electric field amplification, simulating this parameter provides valuable insights into the plasmonic performance of our nanostructures.

To comprehensively evaluate the MIM nanoparticle configuration, we calculated the electric field distribution upon excitation with linearly polarized light in a water medium,

employing PML as boundary conditions (Fig. S1). The permittivity values of Au and SiO_2 were obtained from the COMSOL Multiphysics® material library and varied according to the working wavelength.[30,31] The incident field intensity was set to 1 MW m^{-2}. More details of simulation parameters are listed in Table S1. We systematically investigated three key structural parameters: (i) the core AuNP diameter (D_1), (ii) the silica insulator layer thickness (T), and (iii) the exterior AuNP diameter (D_2).

Fig. 1A illustrates the simulated electric field distribution for an MIM nanoparticle under these conditions. We compared four configurations (Fig. 1B–E): (i) a silica–gold core–shell nanoparticle ($D_1 = 0$, $T = 126$ nm, $D_2 = 13$ nm), and (ii–iv) MIM nanoparticles with varying core AuNP sizes ($D_1 = 120$, 90, and 60 nm) while keeping $T = 3$ nm and $D_2 = 13$ nm. The center-to-center distance of exterior AuNPs was maintained at a minimum of 20 nm to prevent mesh intersection.

Compared to traditional core–shell configurations, where hotspots form between small surface nanoparticles with limited plasmonic activity, our MIM nanoparticles exhibited significantly higher plasmonic enhancement.[32–34] The strongest enhancement was observed within the silica insulator layer; however, due to the asymmetry of the structure, the electric field was also dramatically amplified near the outer surface of the exterior AuNPs. Fig. 1F presents the extinction cross-section spectra of the four nanoparticle configurations over wavelengths ranging from 450 nm to 900 nm. The extinction cross-section, which represents the sum of scattering and absorption cross-sections, serves as an indicator of global plasmonic enhancement. The peak extinction wavelengths for the four configurations were predicted to be 700 nm, 680 nm,

660 nm, and 650 nm, respectively, with the MIM nanoparticle featuring a 120 nm core, a 3 nm silica layer, and a 13 nm exterior AuNP exhibiting the highest plasmonic enhancement. This enhancement arises from two factors: (i) a larger core provides an increased surface area, accommodating more exterior AuNPs to generate additional hotspot regions, and (ii) the size-dependent plasmonic coupling effect, where larger nanoparticle pairs yield stronger plasmonic enhancement.
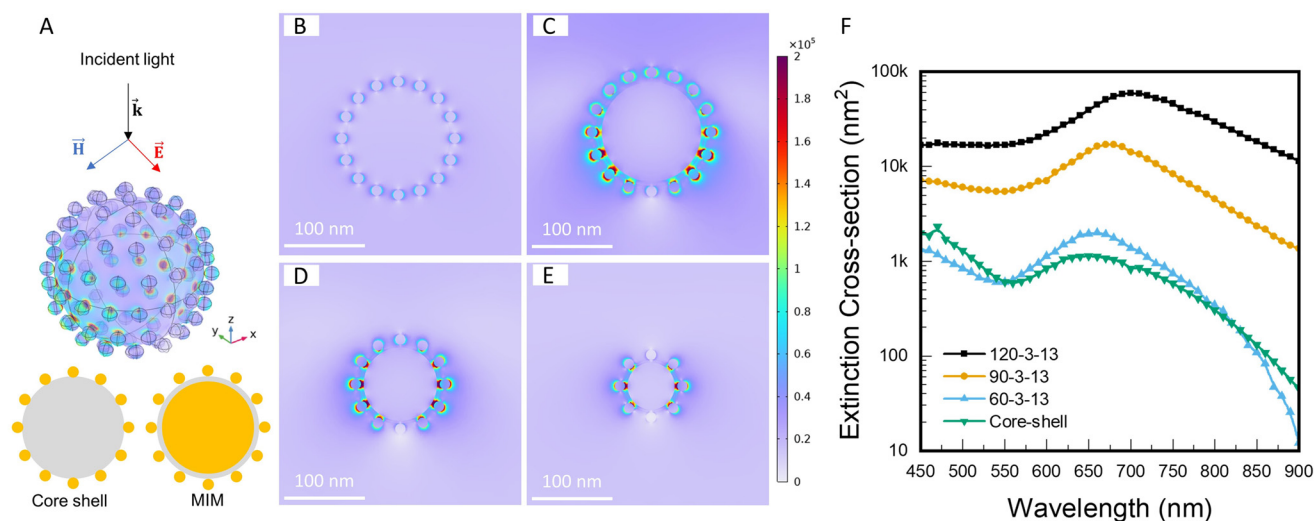
To further elucidate the influence of structural parameters on plasmonic enhancement, we analyzed the electric field distribution along the axis intersecting the core and exterior AuNPs (red line in Fig. 2A). This allowed us to observe two expected peaks: one within the silica insulator layer and another at the outer surface of the exterior AuNP.

• Effect of the core AuNP diameter (D_1): increasing D_1 slightly enhanced the electric field at individual AuNP–AuNP junctions (Fig. 2B), but more significantly, it increased the total surface area, thereby amplifying the overall plasmonic enhancement.

• Effect of the silica layer thickness (T): a thinner silica layer significantly enhanced the local electric field (Fig. 2C), consistent with previous studies demonstrating that closer nanoparticle dimers generate stronger plasmonic effects.[12] When T exceeded 10 nm, the plasmonic enhancement became negligible.

• Effect of the exterior AuNP diameter (D_2): as D_2 increased, the electric field intensity on the exterior AuNP surface initially increased but then decreased beyond an optimal size (Fig. 2D). This is attributed to the weakening of the asymmetric field enhancement effect as D_2 grows larger.
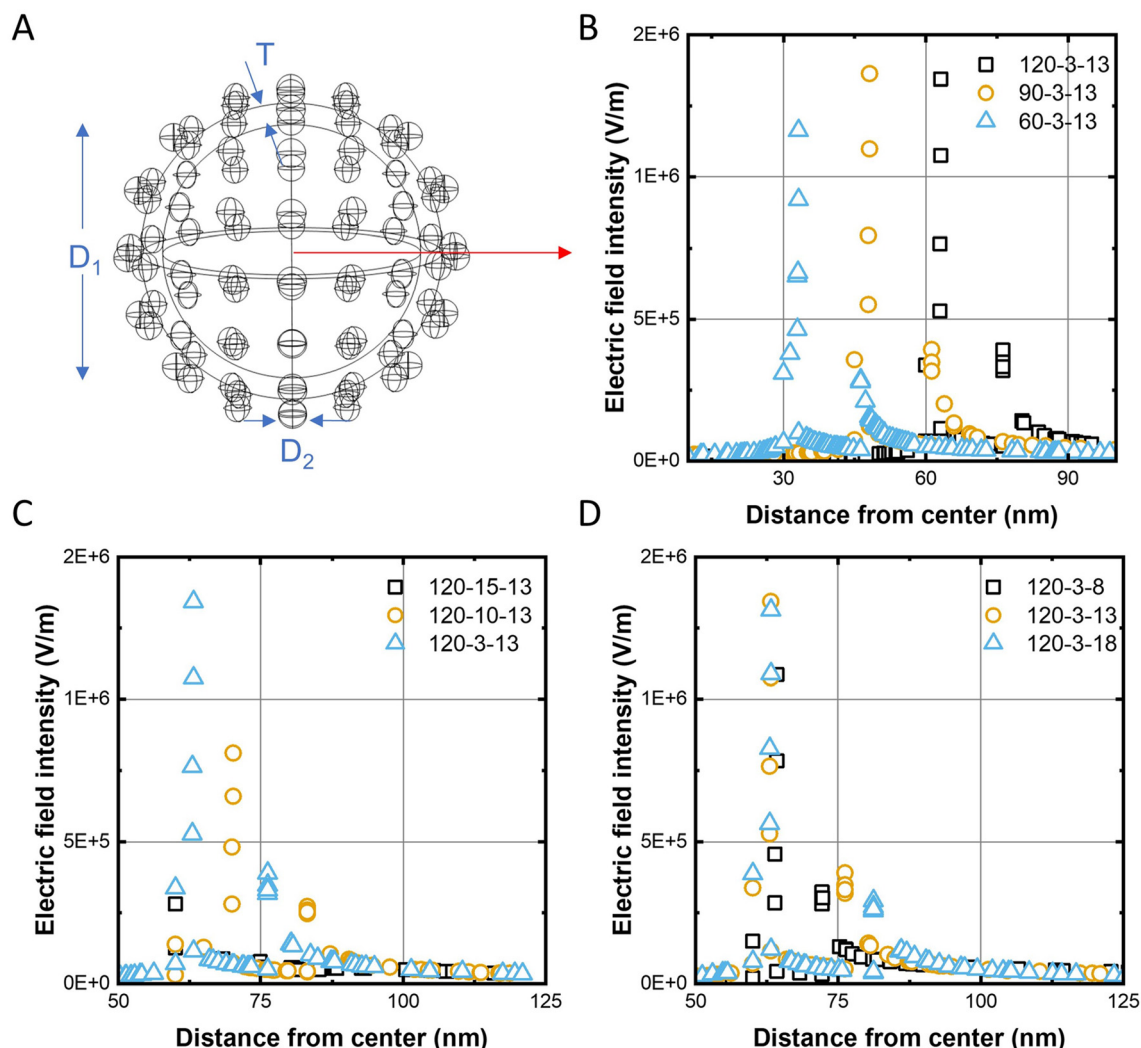
Our findings indicate that optimal plasmonic enhancement is achieved with an MIM nanoparticle featuring a large AuNP

Fig. 1 FEA simulation of electric field enhancement and distribution on MIM nanoparticles. (A) The schematic of the 3D model. (B) Simulation of local electric field distribution for the core−shell structure ($D_1 = 0$, $T = 128$ nm, $D_2 = 13$ nm) in the $X−Z$ plane with 630 nm incident light. (C) Simulation of local electric field distribution for the MIM structure ($D_1 = 120$, $T = 3$ nm, $D_2 = 13$ nm) in the $X−Z$ plane with 630 nm incident light. (D) Simulation of local electric field distribution for the MIM structure ($D_1 = 90$, $T = 3$ nm, $D_2 = 13$ nm) in the $X−Z$ plane with 630 nm incident light. (E) Simulation of local electric field distribution for the MIM structure ($D_1 = 60$, $T = 3$ nm, $D_2 = 13$ nm) in the $X−Z$ plane with 630 nm incident light. The color bar represents electric field intensity (V m^{-1}). (F) The extinction cross-section of different configurations in a wavelength range from 450 nm to 900 nm.

Fig. 2 Electric field distribution under different MIM parameters. (A) The schematic of the 3D model. The red line represents the axis for the electric field intensity distribution study. (B) Electric field distributions in the red line of MIM nanoparticles with different core sizes. (C) Electric field distributions in the red line of MIM nanoparticles with different shell thicknesses. (D) Electric field distributions in the red line of MIM nanoparticles with different exterior AuNP sizes.

core, a thin silica insulator layer, and an appropriately sized exterior AuNP. This rational design provides a robust and reproducible SERS platform, overcoming the limitations of conventional nanoparticle-based SERS sensors.
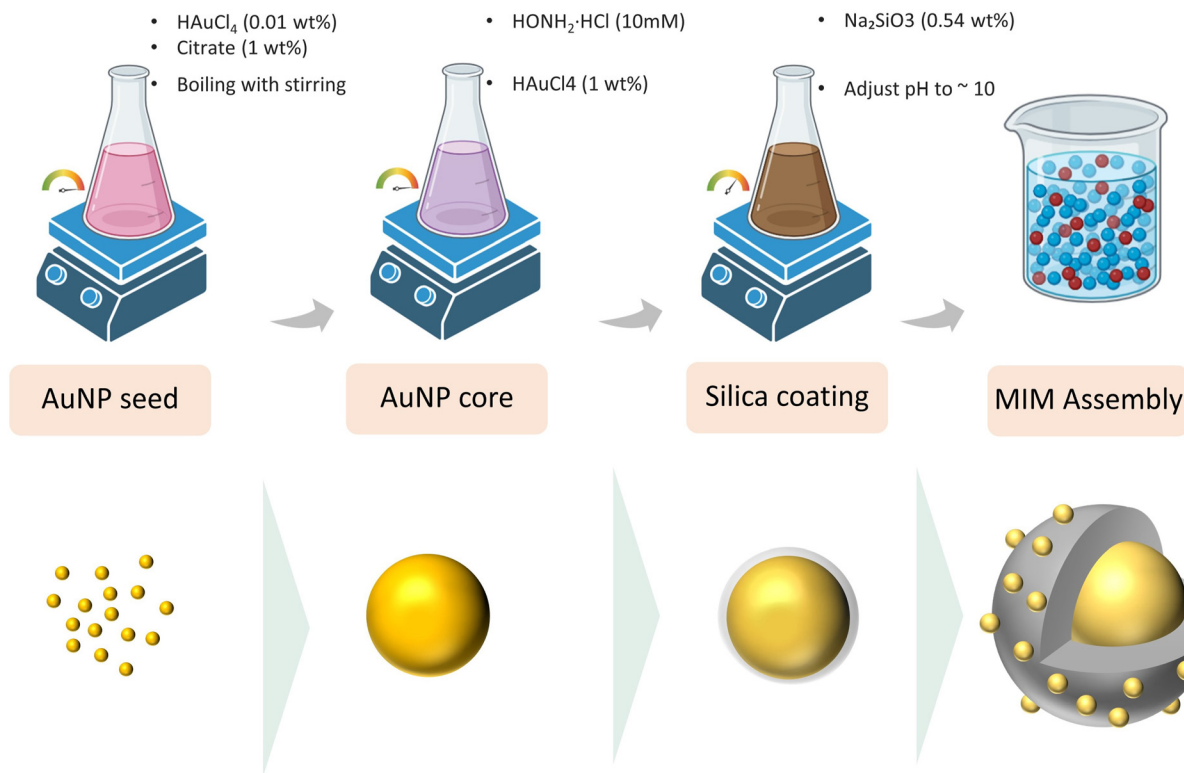
The synthesis process of MIM nanoparticles is illustrated in Fig. 3. Colloidal AuNP seeds were first synthesized using the Turkevich method, where the size of the AuNPs (ranging from 10 to 60 nm) was controlled by adjusting the sodium citrate and chloroauric acid concentrations.[24,25] To produce larger AuNPs for the MIM core, we employed hydroxylamine hydrochloride as a reducing agent. In this process, citrate-reduced AuNPs served as seeds, and hydroxylamine facilitated further growth *via* the surface-catalyzed reduction of Au^{3+}. This approach allows precise size control based on the initial seed diameter and the added Au^{3+} concentration, yielding monodisperse nanoparticles with improved uniformity compared to direct citrate reduction.[26] The ultrathin silica coating was initiated by surface activation for silanization using APTMS, followed by silica deposition *via* sodium silicate in an aqueous solution. By optimizing the reaction conditions, *e.g.*, adjusting pH and increasing the temperature from room temperature to 90 °C, the time required for forming an ~4 nm silica shell was reduced from two days to less than one hour.

For AuNP deposition onto the silica surface, conventional deposition–precipitation methods produce AuNPs limited to 2–8 nm, which is insufficient for optimal plasmonic enhancement.[29,35,36] Instead, we directly assembled AuNPs onto the silica surface, guided by colloidal interaction principles.

A major challenge in our study is to achieve the precise overall structure predicted by the FEA simulations *via* self-assembly. A standard practice is to use ligands to induce nano-

Fig. 3 Schematic of the MIM nanoparticle fabrication process, including gold seed synthesis, MIM core growth, ultrathin silica coating, and MIM nanoparticle assembly.

particle self-assembly. However, in our initial attempt to obtain the desired MIM structure using NaBH$_4$ as the ligand, the resulting structures contained a significant portion of AuNP aggregates instead of the AuNP-decorated MIM nanostructure (see Fig. 4). The failure can be attributed to a lack of quantitative understanding of the molecular driving force of self-assembly in the colloidal system studied herein.

To precisely control the assembly outcome, one needs to discern the complex and entangled interactions in a colloidal solution. Due to the intrinsically different chemical identities of the constituent species, such as inorganic nanoparticles, solvents, salts, ligands, and other small molecules, it may be impractical to consider the roles and interdependence of all chemical species simultaneously. Alternatively, we can extract key influencing factors *via* theoretical approaches from the most fundamental perspectives. Under the Derjaguin–Landau–Verwey–Overbeek (DLVO) theory, forces between two colloidal nanoparticles are governed by the van der Waals (vdW) dispersion and electrostatic interactions.[37–39] In an aqueous solution at a pH value above 3, the silanol groups on the silica surface are deprotonated such that the silica-coated AuNPs are likely negatively charged.[40] By chemically grafting with APTES, the surface charge is then flipped to be positive, whose value can be estimated based on the surface density of silanol groups and APTES (Fig. S2A). On the other hand, bare small AuNPs carry less significant surface charge but are highly attractive to each other due to the strong vdW attractions, thus

exhibiting aggregating behavior without appropriate ligand stabilization. Coating ligands on the small AuNPs not only helps prevent aggregation but also tunes electrostatic interactions that can be used to modulate self-assembly. To rationalize the influences of each type of interaction, identify the key driving force, and propose a solution, we performed the following calculations.
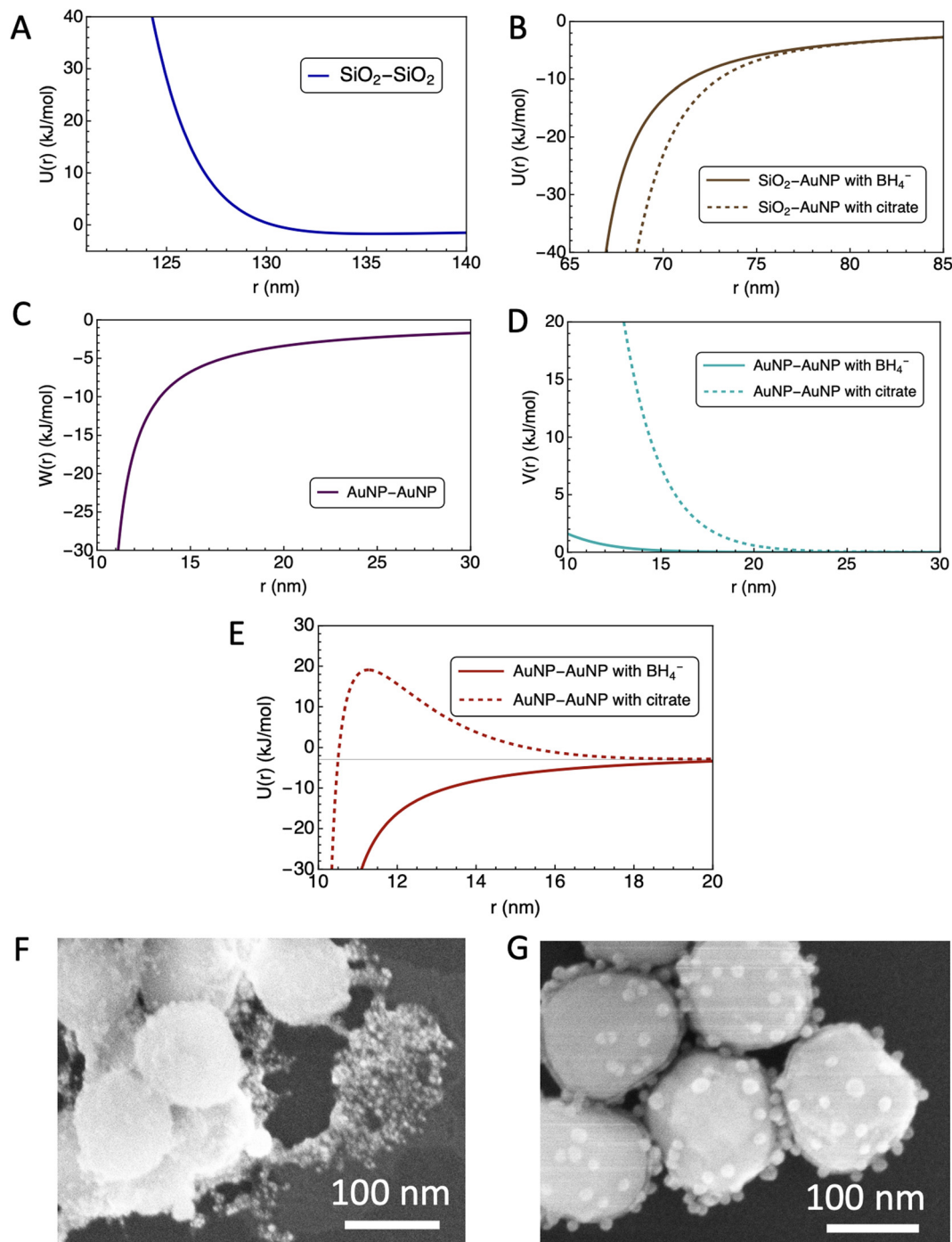
The DLVO theory specifies that:

$$U(r) = W(r) + V(r) \tag{2}$$

where $U(r)$ is the effective potential energy between two particles at a center-to-center separation of r, $W(r)$ is the vdW dispersion and $V(r)$ is the electrostatic interaction. Here, we employ the theoretical approach described in our previous work.[41] The vdW interactions depend on the materials and sizes of the colloidal particles and can be calculated from Lifshitz's theory:[42]

$$W(r) = \\ -\frac{A}{6}\left(\frac{2R_1R_2}{r^2-(R_1+R_2)^2}+\frac{2R_1R_2}{r^2-(R_1-R_2)^2}+\ln\left(\frac{r^2-(R_1+R_2)^2}{r^2-(R_1-R_2)^2}\right)\right) \tag{3}$$

where A is the Hamaker constant that depends on particle species, R_1 and R_2 are the radii of interacting particles, and r is the center-to-center distance between two particles.

Fig. 4 Theoretical calculations of particle-to-particle interactions and TEM images of assembly with different ligands on AuNPs. (A) The effective potential energy profile as a function of the center-to-center distance r between two large SiO_2-coated Au nanoparticles. (B) The effective potential energy profiles between a large SiO_2-coated Au nanoparticle and an AuNP with different ligands. (C) The vdW interaction between two small AuNPs. (D) The electrostatic interaction between two AuNPs with different ligands. (E) The effective potential energy profiles between two small AuNPs with different ligands are obtained by summing up the values in (C) and (D). TEM images of assembly with (F) $NaBH_4$ and (G) sodium citrate as ligands, respectively.

Electrostatic interactions were modeled using a sphere-to-sphere approach, given by:[43]

$$V(r) = \varepsilon \left(\frac{k_B T}{e} \right) y^2 \frac{R_1 R_2}{r^2} \ln \left(1 + e^{-\kappa(r - R_1 - R_2)} \right) \quad (4)$$

where ε is the dielectric constant, k_B is the Boltzmann constant, T is the temperature, e is the elementary charge, y is the absolute surface potential, κ is the Debye screening parameter depending on the electrolyte, R_1 and R_2 are the nanoparticle radii, and r is the center-to-center distance between two par-

ticles. The Debye screening parameter depends on the valency and concentration of the salt used in the aqueous solution:

$$\kappa = \left(\frac{2\rho e^2}{\varepsilon k_B T}\sum_i^x z_i^2\right)^{\frac{1}{2}} \tag{5}$$

where ρ is the salt concentration, and x_i and z_i are the fraction and charge of ions. The electrostatic interaction is critically influenced by the surface potential y, whose value is determined by the surface charge density q, and thus ligand coverage. We can obtain y from the modified Grahame's equation:[44]

$$q = \frac{2\varepsilon k_B T}{ez}\kappa\left(2\,\sinh\left(\frac{\Psi_s}{2}\right) + \frac{4}{\kappa R}\tanh\left(\frac{\Psi_s}{4}\right)\right) \tag{6}$$

and

$$\Psi_s = \frac{ezy}{2k_B T} \tag{7}$$

With the parameters that reflect assembly conditions (Table S2), these equations will generate effective potential energy profiles between two nanoparticles, from which we can find the contributing factor for small AuNP aggregations with NaBH$_4$ and redesign the assembly conditions.

First, we evaluated the effective potentials between small AuNPs and between a small AuNP and the large silica-coated AuNP (labeled as SiO$_2$ in Fig. 4). We used 1.35×10^{-19} J and 1.02×10^{-20} J for the Hamaker constant for Au and SiO$_2$.[45,46] We calculated the surface potential y for the SiO$_2$ nanoparticle based on the grafted ATPES charge density of -0.096 C m^{-2}, as illustrated in Table S2. Similarly, we estimated the charge density carried by BH$_4^-$-coated AuNPs to be 0.24 C m^{-2} and calculated the electrostatic interaction as a function of particle separation accordingly. The most relevant energy profiles are given in Fig. 4A–E. We find that, due to the low charge density carried by NaBH$_4$, the electrostatic repulsion between AuNPs (i.e., the solid line in Fig. 4D) cannot overcome the large vdW attraction intrinsically to Au (i.e., Fig. 4C), thus leading to attraction and aggregation (Fig. 4E and F).

Learning from the DLVO theory, we find that, to achieve the controlled MIM assembly, we need to search for a balance where the exterior AuNPs and SiO$_2$ surfaces carry opposite charges to induce attraction, while the interactions between two AuNPs and two SiO$_2$-coated AuNPs, respectively, must remain sufficiently repulsive to prevent aggregation. We proposed replacing the ligand for AuNPs from NaBH$_4$ to sodium citrate since it not only energetically favors Au(111) (i.e., the representative surface on a small AuNP) and thus increases surface coverage but also significantly increases the charge density per area (Fig. S2B and C).[47] Our theoretical calculations of the effective interactions between AuNPs, using a surface coverage of 3 citrate molecules per nm^2,[48] is shown as the dashed red line in Fig. 4E, which suggests unlikely AuNP aggregation due to a repulsive barrier. In addition, the more negatively charged AuNPs are more attracted to the positively charged SiO$_2$-coated AuNPs, shown as the dashed brown line in Fig. 4B, which further induces attachment of the small

AuNP on the large SiO$_2$-coated AuNPs. Our experimental results yield the expected outcome, i.e., a uniform AuNP distribution on the silica surface (Fig. 4F).
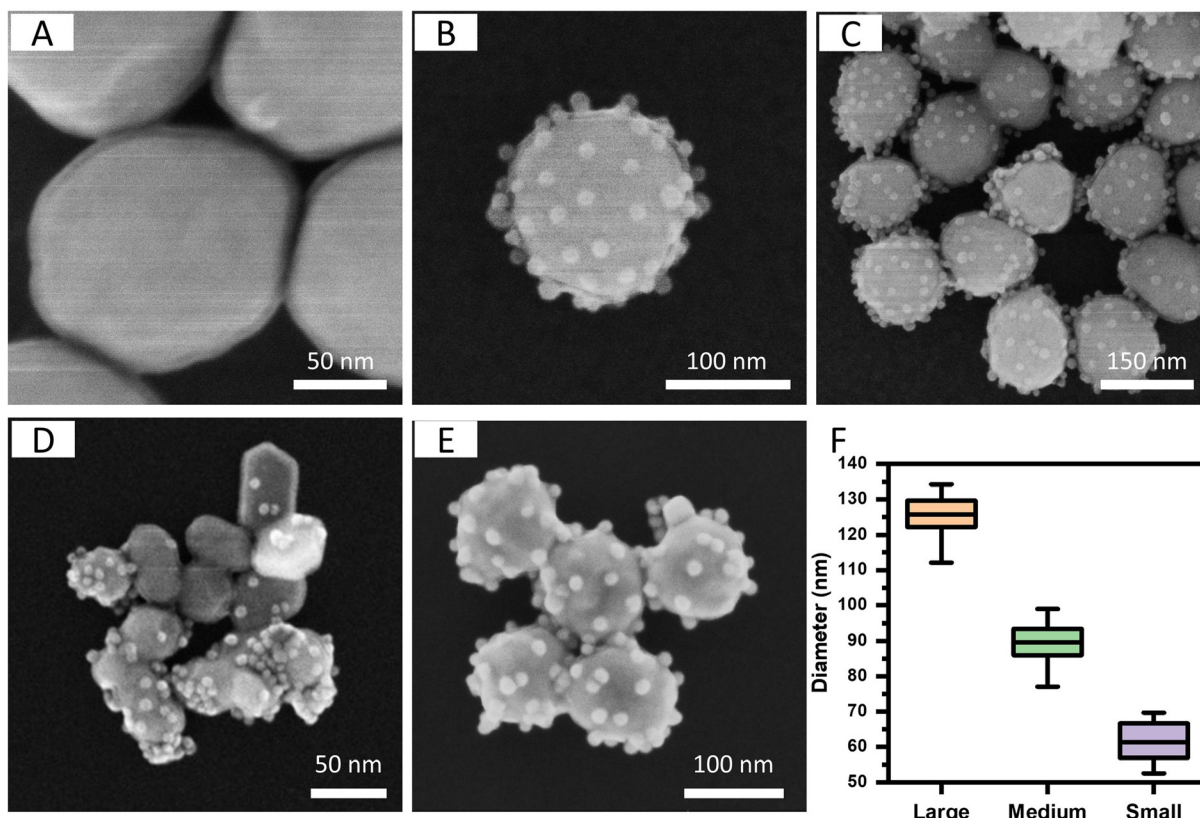
By carefully tuning assembly parameters – including surface ligand chemistry, salt concentration, pH, and particle size – we successfully synthesized MIM nanoparticles in three distinct size configurations, as shown in Fig. 5. We synthesized three MIM nanoparticle cores with different sizes, each coated with a silica shell averaging 3.6 nm in thickness (Fig. 5A). The ultrathin silica layer was further confirmed by TEM characterization and elemental mapping using EDS, as shown in Fig. S3. The assembly of large MIM nanoparticles, with randomly yet uniformly distributed exterior AuNPs, is shown in Fig. 5B, while Fig. 5C provides a broader field-of-view image. Fig. 5D and E present the small and medium-sized MIM nanoparticles. Their average core sizes are 124 nm, 89 nm and 62 nm, respectively (Fig. 5F). The exterior AuNPs have an average diameter of 13 nm. Notably, as the core-to-exterior AuNP size ratio decreases, the distribution of exterior AuNPs becomes less uniform. In the smaller MIM nanoparticles, slight clustering and pinhole defects are observed, indicating a size-dependent assembly behavior. Additionally, we found that the concentration of APTES plays a critical role in modulating surface AuNP loading: increasing APTES concentration leads to a higher number of attached AuNP satellites, reaching an average of ∼52 per MIM nanoparticle (Fig. S4). These structural variations are further reflected in the absorbance spectra of the three MIM nanoparticle types, as shown in Fig. 6.

To evaluate the SERS performance of the MIM nanoparticles, we first validated their activity using a standardized probe molecule, 4-nitrothiophenol (4-NTP), which features distinct Raman fingerprints and well-documented enhancement factors. The spatial uniformity and signal reproducibility of the MIM-based SERS platform were further confirmed through 2D Raman mapping (Fig. S5), while the calculated enhancement factor is detailed in the SI and presented in Fig. S6. To investigate the influence of the silica shell thickness on hotspot accessibility and overall SERS enhancement, we synthesized MIM nanoparticles with silica shells of approximately 6.9 nm, 3.6 nm, and ∼2 nm. STEM images of the Au@SiO$_2$ cores and SEM images of the assembled MIM structures are shown in Fig. S7A–F. The corresponding SERS spectra of 4-NTP obtained from these MIM variants are displayed in Fig. S7G and H. The results demonstrate that thinner silica shells yield stronger SERS signals, in agreement with FEA simulations predicting higher electric field enhancement at reduced core–satellite distances. However, when the shell thickness is reduced to ∼2 nm, structural defects such as pinholes[26] and incomplete coverage become prominent (Fig. S7F), compromising uniformity and potentially diminishing signal consistency. Based on this tradeoff between enhancement and structural reliability, we selected a silica shell thickness of 3.6 nm as the optimal configuration, offering both robust enhancement and reproducible MIM assembly.
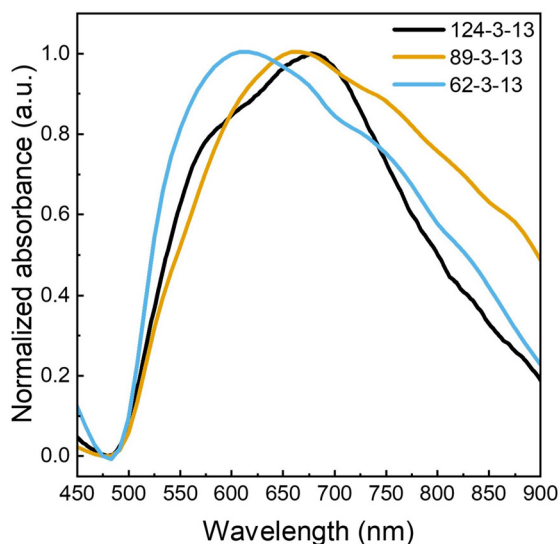
Following this validation, we applied the MIM sensor – specifically, the large MIM configuration (core diameter $D_1 =$

Fig. 5 Characterization of MIM nanoparticles. (A) SEM image showing a uniform and ultrathin silica layer coated on the surface of 120 nm AuNPs. (B) SEM image of a self-assembled MIM nanoparticle (D_1 = 120, T = 3 nm, D_2 = 13 nm). (C) SEM image of MIM nanoparticles (D_1 = 124, T = 3 nm, D_2 = 13 nm) with a larger field of view. (D) SEM image of small MIM nanoparticles (D_1 = 62, T = 3 nm, D_2 = 13 nm). (E) SEM image of medium MIM nanoparticles (D_1 = 89, T = 3 nm, D_2 = 13 nm). (F) Core AuNP size distribution for the three types of MIM nanoparticles.
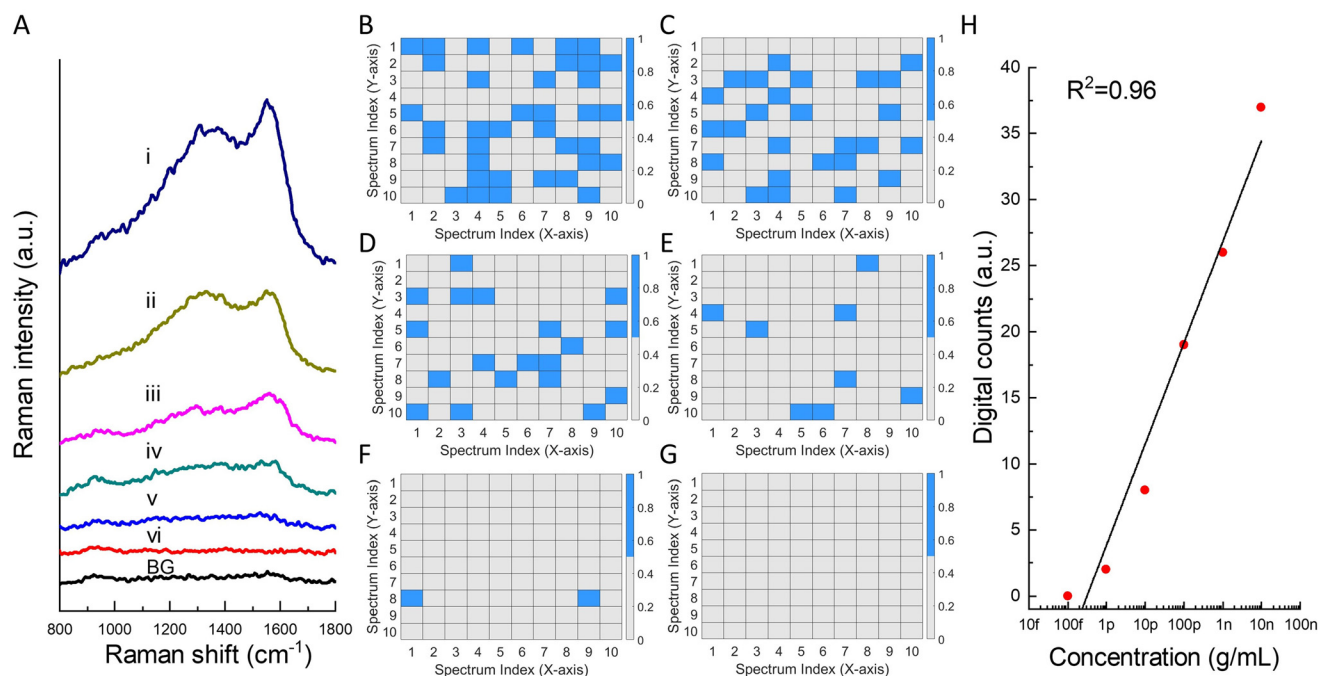

Fig. 6 Absorbance spectra of the three MIM nanoparticles.

124 nm, silica shell thickness T = 3.6 nm, satellite AuNP diameter D_2 = 13 nm) – to detect ciprofloxacin, a fluoroquinolone antibiotic, in a label-free manner. The analyte solutions were mixed with the MIM nanoparticle suspension at a 1 : 10 ratio, and 10 μL of the resulting mixture was used for SERS measurements.

SERS spectra were collected for ciprofloxacin concentrations ranging from 10 ng mL^{-1} to 100 fg mL^{-1}, with the representative spectra shown in Fig. 7A. The Raman spectra exhibited distinct characteristic peaks at 1309.94 cm^{-1}, 1381.02 cm^{-1}, 1488.49 cm^{-1}, and 1570.72 cm^{-1}, consistent with previously reported values. The peak at 1570.72 cm^{-1} corresponds to the C=O stretching vibration and C–C stretching of the pyridine ring, while the peak at 1488.49 cm^{-1} is associated with the O–H in-plane bending and C–C stretching modes.[49] The peak at 1381.02 cm^{-1} is attributed to a combination of CH$_2$ wagging and C–C stretching, while the peak at 1309.94 cm^{-1} is linked to the twisting deformation of CH$_2$ groups.[49–51]

To assess the quantitative molecular sensing capability of the MIM nanoparticles, SERS mapping was performed across various ciprofloxacin concentrations. However, at lower concentrations, we observed significant Raman intensity fluctuations, which can be attributed to variations in molecular orientation and the heterogeneous electromagnetic field distribution within the MIM's hotspots.[13,14] These fluctuations lead to high variability in signal intensity, rendering conventional Raman peak-based calibration methods unreliable for accurate quantification at ultralow concentrations. To overcome these

Fig. 7 SERS spectra of ciprofloxacin using the MIM molecular sensor, and the calibration based on the digitalization process. (A) Representative Raman spectra of ciprofloxacin with a concentration of 10 ng mL^{-1} (i), 1 ng mL^{-1} (ii), 100 pg mL^{-1} (iii), 10 pg mL^{-1} (iv), 1 pg mL^{-1} (v) and 100 fg mL^{-1} (vi). The last spectrum represents the background (BG). (B–G) digital mapping for ciprofloxacin concentration ranging from 10 ng mL^{-1} to 100 fg mL^{-1}. The blue cells correspond to positive signals, while the white cells correspond to negative signals. (H) Digital calibration curve for ciprofloxacin at extremely low concentrations.

limitations, we employed a digital SERS analysis approach, inspired by the principles of digital bioassays.[14,52] The core idea behind digital assays is to partition an extremely dilute solution into small detection volumes, allowing individual signal detection events to be interpreted as arising from single molecules. By leveraging the enhanced plasmonic properties of MIM nanoparticles, this approach enables reproducible quantification of ultralow analyte concentrations, with sensitivity constrained only by Poisson noise in the measurement process.

In our experimental setup, a 50× objective lens (0.5 NA) was used to acquire Raman spectra in a point-by-point mapping mode (10 × 10 grid, totaling 100 measurements) over a 50 × 50 μm^2 area. The monodisperse nature of the MIM nanoparticles ensured homogeneous dispersion within the liquid sample, leading to uniform molecule–hotspot interactions throughout the scanning region.

For digitization, each acquired spectrum was categorized as positive ('1') or negative ('0') based on the intensity of a predefined Raman characteristic peak. The maximum intensity (I_{max}) within the characteristic peak window was extracted after applying despiking, Savitzky–Golay smoothing, and baseline correction by a penalized least-squares approach.[53] The ciprofloxacin signature peak window (1560 cm^{-1}–1580 cm^{-1}) was used to determine I_{max}. To classify spectra as either positive or negative, I_{max} was compared against threshold intensity (I_t), which was experimentally determined as $I_t = \bar{x} + 10\sigma$, where $\bar{x}$ is the mean intensity and σ is the standard deviation within a

non-characteristic spectral window (940 cm^{-1}–970 cm^{-1}), chosen to avoid interference from Raman peaks or background noise. A crucial requirement for digital SERS detection is the presence of well-defined, interference-free characteristic peaks to ensure unambiguous molecule identification. By converting analog intensity values into binary (1/0) signals, the concentration of ciprofloxacin can be quantified based on the number of positive detection out of 100 measurement points.

Fig. 7B–G present the digitized SERS maps obtained for ciprofloxacin concentrations ranging from 10 ng mL^{-1} to 100 fg mL^{-1}. Each blue pixel represents a detection event ($I_{max} > I_t$), signifying the presence of ciprofloxacin molecules, while gray pixels correspond to null detection. The digital counts (*i.e.*, the number of '1' signals out of 100 total measurements) were plotted against ciprofloxacin concentration, yielding a linear digital calibration curve (Fig. 7H). This digital SERS approach significantly extends the linear detection range down to 1 pg mL^{-1}, enabling reliable quantification at ultralow concentrations. These results show that MIM nanoparticles combined with digital SERS analysis can be used to directly quantify ciprofloxacin at ultralow concentrations without requirements for preconcentration and separation steps.

Conclusion

In conclusion, by integrating FEA-guided nanoparticle design, precise synthesis, and digital SERS quantification, we estab-

lished a robust framework for highly sensitive and reproducible molecular detection. We first employed FEA simulations to investigate the plasmonic properties of MIM nanoparticles and determine the optimal structural configuration for maximizing electromagnetic field enhancement. The FEA simulations guided the selection of an optimal core size, silica shell thickness, and exterior AuNP arrangement, ensuring maximal plasmonic enhancement and efficient hotspot formation. Specifically, the simulations revealed that near-field enhancement is maximized with a larger Au core, a thinner silica shell, and appropriately sized exterior AuNPs. Specifically, the analysis identified an optimal configuration with a 120 nm core, a uniform 3 nm silica shell, and well-distributed 13 nm exterior AuNPs, which ensures efficient hotspot formation while minimizing signal suppression caused by excessive clustering. Guided by these insights, we synthesized MIM nanoparticles with three different core sizes (124 nm, 89 nm, and 62 nm) while maintaining a uniform silica shell thickness of ~3.6 nm.

In parallel, we incorporated colloidal force calculations based on the DLVO theory to provide insights into the self-assembly structures of AuNP-decorated silica–Au core–shell MIM nanoparticles. Based on the characteristic nanoparticle information, such as size, material, ligand, and their coverage, we quantified the vdW attractions and electrostatic repulsions among colloidal nanoparticles. Based on the theoretical calculations, we identified an optimal balance of interparticle forces using sodium citrate as the ligand to achieve optimized MIM nanoparticles with uniform exterior AuNP distribution while minimizing undesirable aggregation or pinhole formation. Experimental characterization confirmed the monodispersity of MIM nanoparticles, validating both theoretical predictions and fabrication reproducibility.

Furthermore, digital SERS analysis provided a robust and quantifiable detection strategy at ultralow analyte concentrations, overcoming signal fluctuations associated with traditional intensity-based measurements. To evaluate the SERS sensing capability of the MIM nanoparticles, we employed the optimal large-core configuration (D_1 = 124 nm, T = 3.6 nm, D_2 = 13 nm) to detect ciprofloxacin at ultralow concentrations. While the Raman spectra exhibited characteristic peaks corresponding to ciprofloxacin, intensity fluctuations were observed at low concentrations due to molecular orientation variability and heterogeneous hotspot distribution. To address these limitations, we implemented a digital SERS approach, which converts Raman signals into binary detection events based on a predefined intensity threshold. This method enabled reliable detection, extending the quantifiable concentration range down to 1 pg mL^{-1}, significantly improving sensitivity and reproducibility compared to conventional intensity-based calibration. The established digital calibration curve demonstrated excellent linearity, enabling reliable molecular detection down to the picogram per milliliter range. This integrated approach, *i.e.*, combining computational modeling, colloidal assembly principles, and experimental validation, highlights the potential of MIM-based digital SERS platforms for next-generation molecular sensing

applications, particularly in biosensing, environmental monitoring, and medical diagnostics.

This study highlights the potential of computationally driven nanomaterial synthesis for advancing biomedical diagnostics, environmental sensing, and pharmaceutical analysis. Future research may focus on refining FEA models for additional molecular targets, improving nanoparticle functionalization strategies for enhanced selectivity, and expanding the digital SERS approach to multiplexed detection platforms.

Conflicts of interest

The authors declare no competing financial or non-financial interests.

Data availability

The data supporting this article have been included as part of the SI. The methods and parameters used in FEA simulations and colloidal force calculations, as well as supplementary figures, are provided in the SI. Supplementary information is available. See DOI: **https://doi.org/10.1039/d5nr03536h**.

Code availability: the algorithm for Raman spectra analysis is implemented in MATLAB™, which is available on GitHub (**https://github.com/JunhuZhou/MIM-SERS**).

Acknowledgements

References

1 S. Qiu, *et al.*, Small molecule metabolites: discovery of biomarkers and therapeutic targets, *Signal Transduction Targeted Ther.*, 2023, **8**(1), 132, DOI: **10.1038/s41392-023-01399-3**.

2 J. Zhou, Z. Wu, C. Jin and J. X. J. Zhang, Machine learning assisted dual-functional nanophotonic sensor for organic pollutant detection and degradation in water, *npj Clean Water*, 2024, **7**(1), 3, DOI: **10.1038/s41545-023-00292-4**.

3 Z. Hua, T. Yu, D. Liu and Y. Xianyu, Recent advances in gold nanoparticles-based biosensors for food safety detection, *Biosens. Bioelectron.*, 2021, **179**, 113076, DOI: **10.1016/j.bios.2021.113076**.

4 E. M. Dief, P. J. Low, I. Díez-Pérez and N. Darwish, Advances in single-molecule junctions as tools for chemical and biochemical analysis, *Nat. Chem.*, 2023, **15**(5), 600–614, DOI: **10.1038/s41557-023-01178-1**.

5 B. Su, *et al.*, Fluonanobody-based nanosensor via fluorescence resonance energy transfer for ultrasensitive detection of ochratoxin A, *J. Hazard. Mater.*, 2022, **422**, 126838, DOI: **10.1016/j.jhazmat.2021.126838**.

6 J. Hu, F. Liu, Y. Chen, G. Shangguan and H. Ju, Mass Spectrometric Biosensing: A Powerful Approach for Multiplexed Analysis of Clinical Biomolecules, *ACS Sens.*, 2021, **6**(10), 3517–3535, DOI: **10.1021/acssensors.1c01394**.

7 H. Liu, *et al.*, Molecularly Imprinted Electrochemical Sensors Based on Ti3C2Tx-MXene and Graphene Composite Modifications for Ultrasensitive Cortisol Detection, *Anal. Chem.*, 2023, **95**(44), 16079–16088, DOI: **10.1021/acs.analchem.3c01715**.

8 A. Orlando, *et al.*, A Comprehensive Review on Raman Spectroscopy Applications, *Chemosensors*, 2021, **9**(9), 262, DOI: **10.3390/chemosensors9090262**.

9 H. K. Lee, *et al.*, Designing surface-enhanced Raman scattering (SERS) platforms beyond hotspot engineering: Emerging opportunities in analyte manipulations and hybrid materials, *Chem. Soc. Rev.*, 2019, **48**(3), 731–756, DOI: **10.1039/c7cs00786h**.

10 C. Zong, *et al.*, Surface-Enhanced Raman Spectroscopy for Bioanalysis: Reliability and Challenges, *Chem. Rev.*, 2018, **118**(10), 4946–4980, DOI: **10.1021/acs.chemrev.7b00668**.

11 S. Y. Ding, *et al.*, Nanostructure-based plasmon-enhanced Raman spectroscopy for surface analysis of materials, *Nat. Rev. Mater.*, 2016, **1**(6), 16021, DOI: **10.1038/natrevmats.2016.21**.

12 P. G. Etchegoin and E. C. Le Ru, A perspective on single molecule SERS: Current status and future challenges, *Phys. Chem. Chem. Phys.*, 2008, **10**(40), 6079–6089, DOI: **10.1039/b809196j**.

13 D. P. Dos Santos, M. L. A. Temperini and A. G. Brolo, Intensity Fluctuations in Single-Molecule Surface-Enhanced Raman Scattering, *Acc. Chem. Res.*, 2019, **52**(2), 456–464, DOI: **10.1021/acs.accounts.8b00563**.

14 C. D. L. de Albuquerque, R. G. Sobral-Filho, R. J. Poppi and A. G. Brolo, Digital Protocol for Chemical Analysis at Ultralow Concentrations by Surface-Enhanced Raman Scattering, *Anal. Chem.*, 2018, **90**(2), 1248–1254, DOI: **10.1021/acs.analchem.7b03968**.

15 H. Liu, Q. Li, M. Li, S. Ma and D. Liu, In Situ Hot-Spot Assembly as a General Strategy for Probing Single Biomolecules, *Anal. Chem.*, 2017, **89**(9), 4776–4780, DOI: **10.1021/acs.analchem.7b00461**.

16 N. H. Kim, *et al.*, Smart SERS Hot Spots: Single Molecules Can Be Positioned in a Plasmonic Nanojunction Using Host-Guest Chemistry, *J. Am. Chem. Soc.*, 2018, **140**(13), 4705–4711, DOI: **10.1021/jacs.8b01501**.

17 X. Bi, D. M. Czajkowsky, Z. Shao and J. Ye, Digital colloid-enhanced Raman spectroscopy by single-molecule counting, *Nature*, 2024, **628**(8009), 771–775, DOI: **10.1038/s41586-024-07218-1**.

18 F. Schuknecht, K. Kołątaj, M. Steinberger, T. Liedl and T. Lohmueller, Accessible hotspots for single-protein SERS in DNA-origami assembled gold nanorod dimers with tip-to-tip alignment, *Nat. Commun.*, 2023, **14**(1), 7192, DOI: **10.1038/s41467-023-42943-7**.

19 J. Prinz, C. Heck, L. Ellerik, V. Merk and I. Bald, DNA origami based Au-Ag-core-shell nanoparticle dimers with single-molecule SERS sensitivity, *Nanoscale*, 2016, **8**(10), 5612–5620, DOI: **10.1039/c5nr08674d**.

20 T. Wang, *et al.*, Emerging core–shell nanostructures for surface-enhanced Raman scattering (SERS) detection of pesticide residues, *Chem. Eng. J.*, 2021, **424**, 130323, DOI: **10.1016/j.cej.2021.130323**.

21 R. Chen, *et al.*, Trace analysis and chemical identification on cellulose nanofibers-textured SERS substrates using the "coffee ring" effect, *ACS Sens.*, 2017, **2**(7), 1060–1067, DOI: **10.1021/acssensors.7b00403**.

22 W. Wang, Y. Yin, Z. Tan and J. Liu, Coffee-ring effect-based simultaneous SERS substrate fabrication and analyte enrichment for trace analysis, *Nanoscale*, 2014, **6**(16), 9588–9593, DOI: **10.1039/c4nr03198a**.

23 J. Langer, *et al.*, Present and future of surface-enhanced Raman scattering, *ACS Nano*, 2020, **14**(1), 28–117, DOI: **10.1021/acsnano.9b04224**.

24 J. Turkevich, P. C. Stevenson and J. Hillier, A study of the nucleation and growth processes in the synthesis of colloidal gold, *Discuss. Faraday Soc.*, 1951, **11**(c), 55–75, DOI: **10.1039/DF9511100055**.

25 K. C. Grabar, M. B. Hommer, M. J. Natan and R. G. Freeman, Preparation and Characterization of Au Colloid Monolayers, *Anal. Chem.*, 1995, **67**(4), 735–743, DOI: **10.1021/ac00100a008**.

26 J. F. Li, *et al.*, Surface analysis using shell-isolated nanoparticle-enhanced Raman spectroscopy, *Nat. Protoc.*, 2013, **8**(1), 52–65, DOI: **10.1038/nprot.2012.141**.

27 J. F. Li, *et al.*, Shell-isolated nanoparticle-enhanced Raman spectroscopy, *Nature*, 2010, **464**(7287), 392–395, DOI: **10.1038/nature08907**.

28 H. Wang, X. Liu, X. Li, W. Lu and L. Jiang, One–pot Seedless Synthesis of Uniform Gold Nanoshells and Their Photothermal Conversion Property, *ChemistrySelect*, 2016, **1**(4), 659–663, DOI: **10.1002/slct.201600017**.

29 N. Phonthammachai, *et al.*, Synthesis of Contiguous Silica−Gold Core−Shell Structures: Critical Parameters and Processes, *Langmuir*, 2008, **24**(9), 5109–5112, DOI: **10.1021/la703580r**.

30 G. Ghosh, Dispersion-equation coefficients for the refractive index and birefringence of calcite and quartz crystals, *Opt. Commun.*, 1999, **163**(1–3), 95–102, DOI: **10.1016/S0030-4018(99)00091-7**.

31 W. S. M. Werner, K. Glantschnig and C. Ambrosch-Draxl, Optical Constants and Inelastic Electron-Scattering Data for 17 Elemental Metals, *J. Phys. Chem. Ref. Data*, 2009, **38**(4), 1013–1092, DOI: **10.1063/1.3243762**.

32 P. Guo, *et al.*, Plasmonic core-shell nanoparticles for SERS detection of the pesticide thiram: Size- and shape-dependent Raman enhancement, *Nanoscale*, 2015, **7**(7), 2862–2868, DOI: **10.1039/c4nr06429a**.

33 W. Shen, *et al.*, Reliable quantitative SERS analysis facilitated by core-shell nanoparticles with embedded internal standards, *Angew. Chem., Int. Ed.*, 2015, **54**(25), 7308–7312, DOI: **10.1002/anie.201502171**.

34 S. Bock, *et al.*, Highly sensitive near-infrared SERS nanoprobes for in vivo imaging using gold-assembled silica nanoparticles with controllable nanogaps, *J. Nanobiotechnol.*, 2022, **20**(1), 1–12, DOI: **10.1186/s12951-022-01327-7**.

35 V. G. Pol, A. Gedanken and J. Calderon-Moreno, Deposition of gold nanoparticles on silica spheres: A sonochemical approach, *Chem. Mater.*, 2003, **15**(5), 1111–1118, DOI: **10.1021/cm021013+**.

36 H. Cong, R. Toftegaard, J. Arnbjerg and P. R. Ogilby, Silica-Coated Gold Nanorods with a Gold Overcoat: Controlling Optical Properties by Controlling the Dimensions of a Gold–Silica–Gold Layered Nanoparticle, *Langmuir*, 2010, **26**(6), 4188–4195, DOI: **10.1021/la9032223**.

37 E. J. W. Verwey, Theory of the Stability of Lyophobic Colloids, *J. Phys. Colloid Chem.*, 1947, **51**(3), 631–636, DOI: **10.1021/j150453a001**.

38 B. Derjaguin, A theory of interaction of particles in presence of electric double layers and the stability of lyophobe colloids and disperse systems, *Prog. Surf. Sci.*, 1993, **43**(1–4), 1–14, DOI: **10.1016/0079-6816(93)90010-S**.

39 B. Derjaguin and L. Landau, Theory of the stability of strongly charged lyophobic sols and of the adhesion of strongly charged particles in solutions of electrolytes, *Prog. Surf. Sci.*, 1993, **43**(1–4), 30–59, DOI: **10.1016/0079-6816(93)90013-L**.

40 F. S. Emami, *et al.*, Force Field and a Surface Model Database for Silica to Simulate Interfacial Properties in Atomic Resolution, *Chem. Mater.*, 2014, **26**(8), 2647–2658, DOI: **10.1021/cm500365c**.

41 X. Qi, *et al.*, Predictive Theoretical Framework for Dynamic Control of Bioinspired Hybrid Nanoparticle Self-Assembly, *ACS Nano*, 2022, **16**(2), 1919–1928, DOI: **10.1021/acsnano.1c04923**.

42 W. B. Russel, D. A. Saville and W. R. Schowalter, *Dispersion forces, in Colloidal Dispersions*, Cambridge University Press, 1989, pp. 129–161. DOI: **10.1017/CBO9780511608810.008**.

43 J. E. Sader, S. L. Carnie and D. Y. C. Chan, Accurate Analytic Formulas for the Double-Layer Interaction between Spheres, *J. Colloid Interface Sci.*, 1995, **171**(1), 46–54, DOI: **10.1006/jcis.1995.1149**.

44 W. B. Russel, D. A. Saville and W. R. Schowalter, Electrostatic stabilization, in *Colloidal Dispersions*, Cambridge University Press, 1989, pp. 258–309. DOI: **10.1017/CBO9780511608810.011**.

45 L. Bergström, Hamaker constants of inorganic materials, *Adv. Colloid Interface Sci.*, 1997, **70**, 125–169, DOI: **10.1016/S0001-8686(97)00003-1**.

46 M. Götzinger and W. Peukert, Particle Adhesion Force Distributions on Rough Surfaces, *Langmuir*, 2004, **20**(13), 5298–5303, DOI: **10.1021/la049914f**.

47 O. A. Perfilieva, D. V. Pyshnyi and A. A. Lomzov, Molecular Dynamics Simulation of Polarizable Gold Nanoparticles Interacting with Sodium Citrate, *J. Chem. Theory Comput.*, 2019, **15**(2), 1278–1292, DOI: **10.1021/acs.jctc.8b00362**.

48 G. Chong, E. D. Laudadio, M. Wu, C. J. Murphy, R. J. Hamers and R. Hernandez, Density, Structure, and Stability of Citrate 3− and H 2 citrate – on Bare and Coated Gold Nanoparticles, *J. Phys. Chem. C*, 2018, **122**(49), 28393–28404, DOI: **10.1021/acs.jpcc.8b09666**.

49 R. K. Sinha and P. Biswas, Structural elucidation of Levofloxacin and Ciprofloxacin using density functional theory and Raman spectroscopy with inexpensive lab-built setup, *J. Mol. Struct.*, 2020, **1222**, 128946, DOI: **10.1016/j.molstruc.2020.128946**.

50 A. I. M. Athamneh, R. A. Alajlouni, R. S. Wallace, M. N. Seleem and R. S. Senger, Phenotypic Profiling of Antibiotic Response Signatures in Escherichia coli Using Raman Spectroscopy, *Antimicrob. Agents Chemother.*, 2014, **58**(3), 1302–1314, DOI: **10.1128/AAC.02098-13**.

51 C. Liu, L. Müller-Bötticher, C. Liu, J. Popp, D. Fischer and D. Cialla-May, Raman-based detection of ciprofloxacin and its degradation in pharmaceutical formulations, *Talanta*, 2022, **250**, 123719, DOI: **10.1016/j.talanta.2022.123719**.

52 Y. Zhang and H. Noji, Digital Bioassays: Theory, Applications, and Perspectives, *Anal. Chem.*, 2017, **89**(1), 92–101, DOI: **10.1021/acs.analchem.6b04290**.

53 Z.-M. Zhang, S. Chen and Y.-Z. Liang, Baseline correction using adaptive iteratively reweighted penalized least squares, *Analyst*, 2010, **135**(5), 1138, DOI: **10.1039/b922045c**.